Earth and Planetary Science Letters 466 (2017) 168–180

Contents lists available at ScienceDirect

Earth and Planetary Science Letters

www.elsevier.com/locate/epsl

Phase petrology reveals shallow magma storage prior to large explosive silicic eruptions at Hekla volcano, Iceland

Gregor Weber [a,b,*], Jonathan M. Castro [a]

[a] Johannes Gutenberg-University, Institute for Geosciences, J.-J.-Becher-Weg 21, Mainz, Germany
[b] University of Geneva, Department of Earth Sciences, Rue des Maraîchers 13, Geneva, Switzerland

ARTICLE INFO

Article history:
Received 4 September 2016
Received in revised form 8 March 2017
Accepted 9 March 2017
Available online 28 March 2017
Editor: T.A. Mather

Keywords:
Hekla
phase equilibria
magma storage
plagioclase zoning
deformation

ABSTRACT

Understanding the conditions that culminate in explosive eruptions of silicic magma is of great importance for volcanic hazard assessment and crisis mitigation. However, geological records of active volcanoes typically show a wide range of eruptive behavior and magnitude, which can vary dramatically for individual eruptive centers. In order to evaluate possible future scenarios of eruption precursors, magmatic system variables for different eruption types need to be constrained. Here we use petrological experiments and microanalysis of crystals to clarify the P–T–x state under which rhyodacitic melts accumulated prior to the H3 eruption; the largest Holocene Plinian eruption of Hekla volcano in Iceland. Cobalt-buffered, H_2O-saturated phase equilibrium experiments reproduce the natural H3 pumice phenocryst assemblage (pl > fa + cpx > ilm + mt > ap + zrc) and glass chemistry, at 850 ± 15 °C and P_{H_2O} of 130 to 175 MPa, implying shallow crustal magma storage between 5 and 6.6 km. The systematics of FeO and anorthite ($CaAl_2Si_2O_8$) content in plagioclase reveal that thermal gradients were more important than compositional mixing or mingling within this magma reservoir. As these petrological findings indicate magma storage much shallower than is currently thought of Hekla's mafic system, we use the constrained storage depth in combination with deformation modeling to forecast permissible surface uplift patterns that could stem from pre-eruptive magma intrusion. Using forward modeling of surface deformation above various magma storage architectures, we show that vertical surface displacements caused by silicic magma accumulation at ~6 km depth would be narrower than those observed in recent mafic events, which are fed from a lower crustal storage zone. Our results show how petrological reconstruction of magmatic system variables can help link signs of pre-eruptive geophysical unrest to magmatic processes occurring in reservoirs at shallow depths. This will enhance our abilities to couple deformation measurements (e.g. InSAR and GPS) to petrological studies to better constrain potential precursors to volcanic eruptions.

1. Introduction

Large explosive eruptions of silicic magma constitute perhaps the most dramatic natural phenomena on Earth. Yet to date, only a small number of events with erupted magma volumes >1 km^3 have been scientifically monitored (Lipman and Mullineaux, 1981; Harlow et al., 1996; Jay et al., 2014). Our ability to identify precursors to such eruptions is critical in the context of improved hazards assessments and mitigation of these events, which may develop quickly and be exceedingly explosive (Castro and Dingwell, 2009). Clearly, geophysical signals such as surface deformation and seismicity that serve as harbingers to big eruptions can be monitored (e.g., Parks et al., 2012), and because such signals are controlled by magmatic processes beneath volcanoes (e.g., Castro et al., 2016), investigations of magmatic system variables such as pressure (depth), temperature, and volatile budget, provide critical information to augment modeling and interpretation of monitoring signals, as shown by a number of studies (Muir et al., 2014; Caricchi et al., 2014; Jay et al., 2014).

Muir et al. (2014) used experimental petrology and modeling of surface displacement to show that the recent broad (~70 km) deformation of Uturuncu volcano in the Central Andes is probably caused by intrusion of intermediate magma at mid-crustal rather than shallow (<6 km) depths, while Caricchi et al. (2014) employed thermal and petrological calculations to identify the most likely processes controlling the 1997 to 2008 subsidence of the Okmok caldera (Aleutians). Jay et al. (2014) combined geodetic measurements and petrological microanalysis to "inversely" determine magmatic storage depths (5–9 km) and volume changes

* Corresponding author.
E-mail address: gregor.weber@unige.ch (G. Weber).

http://dx.doi.org/10.1016/j.epsl.2017.03.015

that fed the 2011 eruption at Cordón Caulle (Chile). These examples illustrate the rich potential of petrological studies to identify magma storage positions, geometries, and processes that underpin geophysical monitoring signals at restless volcanoes. However, the rarity of big silicic eruptions and monitoring datasets thereof limits such inversion to being synoptic rather than forecasting in nature. Forward modeling of petrological results—that is the use of experimentally constrained magma depths as *initial* inputs to surface deformation models—is an hitherto unexplored yet fertile approach that could yield forecasts of pre-eruptive deformation. Such an approach is the goal of this paper.

Linking signs of pre-eruptive unrest to the sub-volcanic architecture of magma bodies requires a first-order understanding of the depths over which magmas reside and crystallize in the crust, which may vary substantially across tectonic setting. As this information is completely lacking for highly evolved volcanoes in Iceland, we consider magma dynamics at Hekla volcano, one of the largest centers of explosive volcanism in Iceland. Hekla has produced at least five paroxysmal Holocene eruptions with Volcanic Explosivity Indices of 5 (Jónasson, 2007), and the associated hazards and risks of such large events, were they to repeat, could extend beyond Iceland into Europe. In particular, we performed phase equilibria experiments to constrain the P_{H_2O}–T–fO_2 conditions under which the rhyodacitic magma that fueled the largest Hekla eruption (H3) last equilibrated prior to eruption, and thus to provide an estimate of magma storage depth. We further interrogate chemical zoning profiles in plagioclase phenocrysts to investigate thermal and compositional perturbations in Hekla's H3 pre-eruptive reservoir. We show, using a novel combination of pre-eruptive storage conditions and deformation models, that in contrast to more recent mafic to intermediate eruptions, silicic volcanism at Hekla is shallowly sourced. Shallow magma reservoirs, if perturbed by replenishment events, should generate detectable surface deformation prior to silicic eruptions (e.g., Jay et al., 2014). As rejuvenation of near-solidus evolved magma bodies in the crust can operate on timescales relevant for eruption forecasting (Barker et al., 2016), our study has implications for forecasting eruptions of chemically diverse magma reservoirs at Hekla and other volcanoes with bi-modal eruption tendencies.

2. Hekla volcano: magma storage and studied samples

Hekla volcano in southern Iceland is one of the most active volcanoes in Europe. Indeed, Hekla's Holocene eruption history, as manifested by detailed historical records (Thordarson and Larsen, 2007) and in prehistoric tephra layers (Sverrisdottir, 2007), is marked by two contrasting types of behavior. Well-documented historical eruptions, typically of basaltic andesite composition and volumes <0.22 km^3 DRE, start with an explosive Plinian phase, and are followed by lava effusion. Hekla's activity is also characterized by large, purely explosive dacitic to rhyolitic eruptions. Several such silicic tephra layers have been identified in the geological record: The H5 (6200 BP; 0.7 km^3 DRE), H4 (3830 BP; 1.8 km^3 DRE), HSelsund (3515 BP; 0.4–0.5 km^3 DRE), H3 (2879 BP; 2.2 km^3 DRE) and H1104 (846 BP; 0.61 km^3 DRE).

Recent geodetic monitoring data for Hekla's historical eruptions (Sturkell et al., 2013) implies that such events are fed from a deep crustal magma source, yielding distinctly broad surface deformation patterns around the volcano. A number of geophysical studies have been conducted to estimate the depth of the magma storage region beneath the volcano. Early studies, including repeated electronic distance measurements (Kjartansson and Gronvold, 1983), borehole strain monitoring (Linde et al., 1993), and GPS ground deformation studies (Sigmundsson et al., 1992; Tryggvason, 1994), pointed to a reservoir between 5 and 11 km depth for basaltic andesite eruptions. However, Sturkell et al. (2013) pointed out that these estimates are no longer considered to be reliable, due to a previously unrecognized artefact in the strain data. Deep magma storage is implied by seismic studies, which have not detected molten material in the depth range between 4 and 14 km (Soosalu and Einarsson, 2004). Modeling of GPS (Geirsson et al., 2012) and InSAR time series (Ofeigsson et al., 2011; Sturkell et al., 2013) revealed that magma is accumulating in the lower crust, ranging somewhere between 10 and 24 km depth, feeding the present-day more mafic to intermediate eruptions.

Table 1
Chemical composition of Hekla (H3 eruption) bulk rock and matrix glass determined by XRF and EMPA.

Major elements (wt.%)	H3 whole rock[a]	H3 matrix glass $n = 30$	1 SD
SiO_2	69.93	72.59	0.53
Ai_2O_3	14.72	14.67	0.26
FeO (t)	4.83	3.21	0.07
MnO	0.14	0.12	0.04
MgO	0.13	0.13	0.01
CaO	2.66	2.14	0.07
Na_2O	4.85	4.74	0.18
K_2O	2.33	2.55	0.05
TiO_2	0.34	0.22	0.01
P_2O_5	0.05	0.05	0.02
SO_3	0.02	0.04	0.01
F	–	0.18	0.12
Cl	–	0.05	0.01
LOI	1.19		
Total[b]	99.1	100.6	0.85

[a] Normalized to 100% anhydrous.
[b] Hydrous total.

Samples from the largest Holocene eruption of Hekla volcano (H3) were collected from a proximal (about 8 km from the vent) Plinian fallout deposit, which was dated by Dugmore et al. (1995) with an age of 2879 ± 34 yr. BP (calibrated ^{14}C age). Tephra with a volume of 10 to 12 km^3 (2.2 km^3 Dense Rock Equivalent) was ejected into the atmosphere during this eruption (Larsen and Thorarinsson, 1977). The whole rock geochemistry of the deposit is zoned from rhyodacitic (~68 wt.% SiO_2) in the lower and middle layers to andesitic (~56 wt.% SiO_2) in the uppermost deposit, probably reflecting the injection of a basaltic andesite dyke that also triggered the eruption (Sverrisdottir, 2007). Since we are primarily interested in constraining the equilibrium magma storage conditions of silicic magma at Hekla, we neglect the hybridized parts of the deposit responsible for the chemical zoning in our study. Pumice samples from the lower and middle part of the deposit, which were used in this study, contain a mineral phase assemblage comprising plagioclase > fayalitic olivine + clinopyroxene > titanomagnetite + ilmenite, as well as minor apatite and zircon (Fig. 1). Whole rock pumice and matrix glass analyses of the studied samples are provided in Table 1.

All studied samples are crystal-poor (<10 vol.%), and show a highly vesicular texture and homogeneous rhyolitic groundmass glass composition (72.59 ± 0.53 wt.% SiO_2). The groundmass glass is microlite free in all samples, implying that no crystallization occurred upon rapid ascent of the magma. Plagioclase ($An_{31-48}\,Ab_{54-68}\,Or_{1-2}$) is the most common phenocryst phase and occurs as subhedral fragments or euhedral crystals (100 and 1000 μm). The second most common mineral is euto subhedral fayalitic olivine ($Fo_{12-13}\,Fa_{83-84}\,Te_3$). Clinopyroxene ($Wo_{35-42}\,En_{24-35}\,Fs_{36-45}$) is present in similar amounts and size to fayalite in the analyzed samples. The grains are typically subhedral fragments but euhedral crystals also occur.

Faceted crystal faces are observable on all of the analyzed mineral phases, whereas resorption surfaces or mineral breakdown reaction coronas are sparse in these samples. This textural evidence indicates that the phase assemblage grew from magma at equilib-

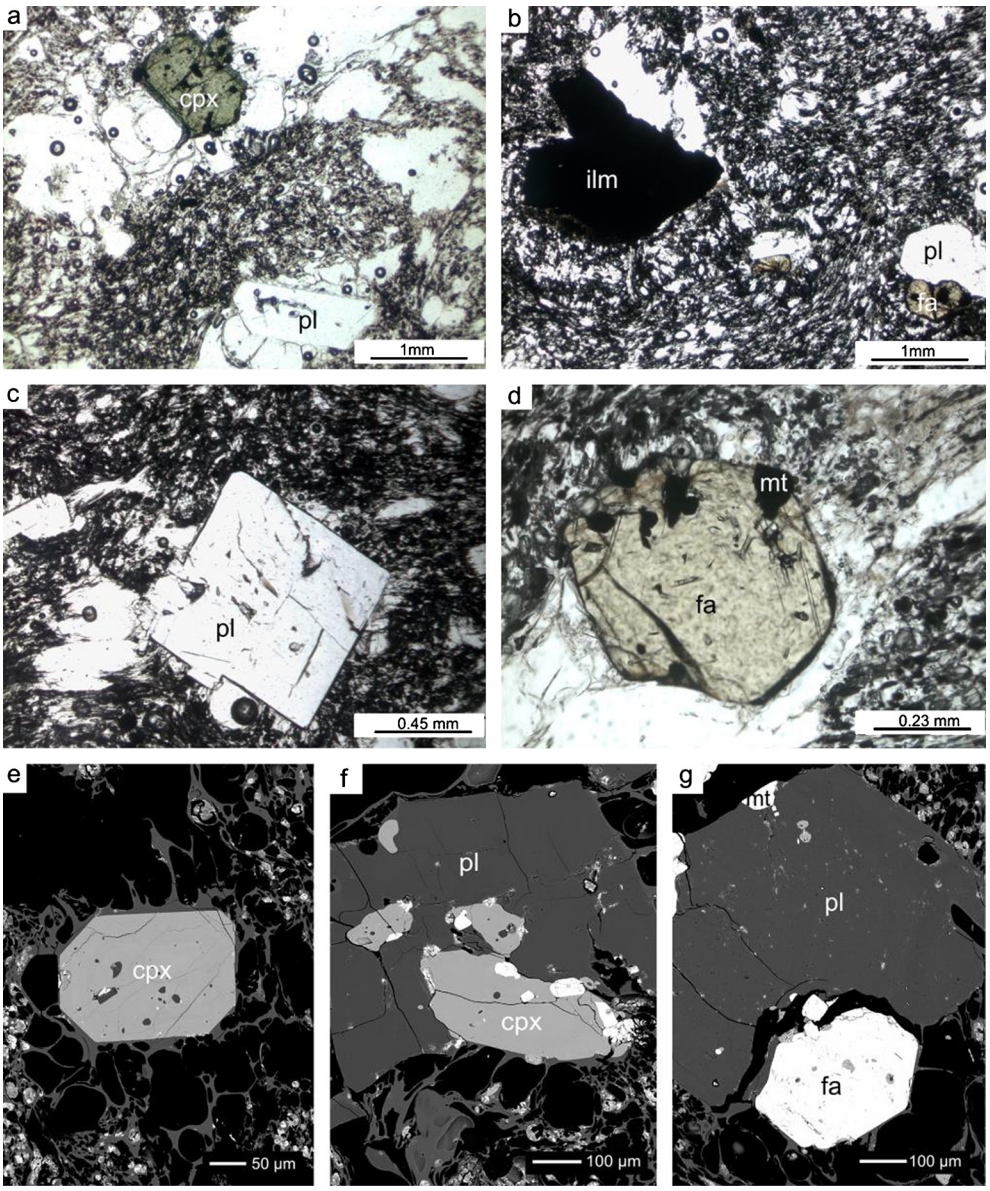

Fig. 1. Representative optical light (a–d) and BSE (e–g) microphotographs of the mineral phase assemblage and textures in Hekla H3 pumice samples. (a) Green clinopyroxene (cpx) and plagioclase (pl). (b) Ilmenite (ilm), plagioclase and fayalitic olivine (fa). (c) Plagioclase (pl) in vesicular groundmass (d) Euhedral fayalitic olivine grain with inclusions of titanomagnetite (mt). (e) Clinopyroxene and highly vesicular matrix glass that is lacking microlites. (f) Glomerocryst of plagioclase and clinopyroxene. (g) Plagioclase, titanomagnetite and fayalite with inclusions of apatite.

rium conditions and that the magma storage conditions prior to eruption were not changed on a timescale sufficient so as to modify magma's phase assemblage (Pichavant et al., 2007).

3. Methods

3.1. Petrological experiments

In order to reconstruct the silicic magma storage conditions beneath Hekla volcano, a series of constant pressure and temperature experiments were carried out to determine the stability fields of the natural phase assemblage in this magma. This approach is broadly similar to that of many previous experimental studies (e.g., Rutherford et al., 1985; Castro et al., 2013; Muir et al., 2014). These experiments were designed to achieve equilibrium among the solid and liquid constituents of the system for a given set of P–T–fO_2 conditions, as it can be expected for a magma reservoir prior to disturbance e.g. by pressurization due to dyke injection and eruption (Pichavant et al., 2007). All experiments were performed at the Johannes-Gutenberg University Mainz, using horizontal tube furnaces and Ni–Co-alloy (Waspaloy) "cold-seal" pressure vessels (autoclaves). H_2O was utilized as a pressurizing medium by way of a rotary vane pump. To fix the oxygen fugacity of the experiment, and to prevent fluid convection, a pure Cobalt metal filler-rod was placed in the free space above the sample capsule within the autoclave in each experiment. Cobalt filler-rods impose the redox conditions at about ΔNNO-1.3 (NNO = Nickel–Nickel Oxide; Matthews et al., 2003), which is roughly equivalent in terms of fO_2 to the quartz–fayalite–magnetite (QFM) buffer and therefore consistent with the presence of ferrous-iron-bearing fayalitic olivine in the rhyodacite (e.g., Scaillet et al., 2016; Supplementary Fig. 1). Redox conditions imposed by Co-rods are furthermore close to previous fO_2 estimates of magma crystallization for the H3 and H4 eruptions of Hekla volcano (ΔNNO ~ -1 to -1.4), as determined from coexisting magnetite and ilmenite pairs by Portnyagin et al. (2012).

Table 2
Set experimental conditions and results for Hekla H3 rhyodacite experiments.

Experiment	Temperature (°C)	Pressure (MPa)	Duration (h)	φ[a] (area %)	Assemblage
H3-2	850	100	119	16	gl pl, fa, cpx, ilm, mt, ap, zrc
H3-3	850	200	94	2	gl pl, cpx, fa, ap, ilm, mt, zrc
H3-5	900	100	192	1	gl cpx, fa, ap, mt, zrc
H3-6	900	50	138	41	gl pl, cpx, fa, ap, ilm, mt, zrc
H3-7	850	50	137	63	gl pl, cpx, fa, ap, mt, zrc
H3-8	850	150	309	8	gl pl, cpx, fa, ap, ilm, mt, zrc
H3-9	750	150	309	47	gl pl, cpx, fa, ap, ilm, mt, zrc
H3-10	950	100	69	0.1	gl ap, ilm, zrc
H3-11	975	50	70	0.3	gl pl, ap, ilm, zrc
H3-12	875	200	70	0.8	gl fa, ap, ilm, zrc
H3-13	900	125	119	–	gl ap, ilm, mt, zrc
H3-14	925	100	98	–	gl ap, ilm, zrc
H3-15	925	80	144	–	gl pl, ap, ilm, zrc
H3-16	950	50	142	–	gl pl
H3-17	900	193	178	–	gl ap, ilm, zrc
H3-18	860	175	98	–	gl cpx, fa, ap, mt, zrc
H3-19	875	125	171	2	gl pl, cpx, fa, ap, mt, zrc
H3-HT1[b]	1030	30	25	–	gl pl, ap, ilm, mt, zrc
H3-20	875	75	314	24	gl pl, fa, cpx, ilm, mt, ap, zrc
H3-21	800	150	312	23	gl pl, fa, cpx, ilm, mt, ap, zrc
HR6	800	100	166	30	gl pl, cpx, fa, ap, ilm, mt, zrc
HR5a	850	125	164	14	gl pl, cpx, fa, ap, ilm, mt, zrc
HR5a_rev	875	150	119	<1	gl fa, ap, mt
HR5b_rev	900	150	164	<1	gl ap, zrc

gl: glass; fa: fayalite; cpx: clinopyroxene; pl: plagioclase; ilm: ilmenite; mt: magnetite; ap: apatite; zrc: zircon
[a] Crystallinity determined by 2D BSE image analysis.
[b] No H_2O added to the starting material.

The starting material for all experiments was a finely ground H3 fallout pumice fragment from the middle part of the deposit. We decanted approximately 50 to 80 mg of the powder in Au capsules along with sufficient distilled water (3–6 mg) to saturate the melt in H_2O (Table 2). The capsules were then welded shut with an acetylene–oxygen torch. To prevent volatile loss during welding, the capsules were wrapped in water-saturated paper, and partly submerged in a larger water reservoir. After welding, the capsules were reheated at about 120 °C and reweighed to ensure that the capsules were reliably sealed. Capsules that showed significant weight loss after welding and reheating were discarded.

Experimental run durations varied between 3 and 13 days, depending on the temperature and P_{H_2O} conditions, to ensure attainment of local equilibrium conditions between melt and phenocryst rims (Pichavant et al., 2007). At the end of an experiment, the autoclaves were first cooled with compressed air for a few minutes, and then rapidly submerged in a cold water bath. We mitigated significant pressure loss upon cooling by overpressurizing the experiments by 30 bars above the target point shortly before the air-cooling phase. After quenching, the capsules were removed and cleaned in an ultrasonic bath, dried and weighed again to check for leakage during the experimental run. The gold capsules were then cut open with a razor blade, and the experimental materials were removed. In each case we observed fluid fizzing out of the capsule when opening the experimental charges. The run products were then prepared for electron probe microanalysis.

The pressure and temperature were monitored daily to ensure stable equilibrium conditions. Pressure was checked by a factory-calibrated Bourdon-tube gauge, and also with a pressure transducer. The associated errors in pressure readings are ±0.5 MPa (Castro et al., 2013). An inconel-sheathed K-type thermocouple was inserted into a bore at the end of the bomb to measure the temperature at a point closest to the capsule. Additionally, an integrated thermocouple inside the furnace measured the temperature in the middle of the autoclave. Little to no thermal gradient was observed between the two temperature readings, although each thermocouple carries an error of ±5 °C.

3.2. Analytical techniques

The chemical compositions of natural and experimental glass (Table 3), as well as mineral phases, were determined using electron probe microanalysis (EPMA; JEOL JXA 8200) at the University of Mainz. Natural silicate mineral analyses were performed on polished sections of 80 µm thickness. Additionally, about 200 plagioclase phenocrysts were separated from lightly crushed pumice in the grain size fractions between 500 µm and 2 mm Natural crystals and experimentally produced materials were mounted in epoxy raisin and polished according to standard methods and coated with ~20 nm carbon prior to EPMA analysis.

For natural and experimental silicate minerals, an acceleration voltage of 15 kV and a current of 12 nA were used. The beam diameter was set to 2 µm and counting times were 20 s for all analyzed elements. 3 to 6 measurements were made on individual phases depending on grain size. If possible, several mineral grains were examined in each experiment. The natural silicate mineral phases were analyzed by compositional traverses (5–10 measurement spots) through individual crystals from polished sections.

High-resolution compositional traverses with distances of up to 10 µm between measurement spots were obtained on plagioclase separates ($n = 47$ crystals) with 15 kV acceleration voltage, probe diameter of 5 µm and 8 nA beam current. Counting times were 25 s for Na, K, Al and Si, 40 s for Ba and Sr, 30 s for Mg and Ca, 60 s for Fe. The compositional zoning pattern of these grains was imaged by back-scattered electrons (BSE).

For all glass analyses an acceleration voltage of 15 keV, sample current of 12 nA, and the following counting times were used: Al 20 s, Fe 40 s, Si 20 s, Ca 20 s, Mg 20 s, Na 15 s, P 25 s, Mn 40 s, Ti 20 s, K 20 s, S 30 s, Cl 25 s and F 40 s. The probe diameter was set to either 5 or 10 µm. Na measurements were made first in the sequence with a defocused beam of 10 µm and reduced current of 6 nA to mitigate diffusion. Additionally, offline corrections similar to those done by Castro et al. (2013) were employed based on the measured decay of Na counts with time (e.g. Devine et al., 1995). We analyzed 10 randomly distributed measurement spots over each experimental glass and 3 natural pumice thin sections.

Table 3
Electron microprobe analyses of the experimental glasses produced from Hekla 3 starting material.

Experiment[a]	Na_2O	SiO_2	CaO	FeO	P_2O_5	F	MgO	K_2O	MnO	Cl	Al_2O_3	TiO_2	Total[b]
H3-1 ($n = 10$)	5.64	71.22	2.33	2.44	0.045	0.200	0.118	2.37	0.119	0.046	15.30	0.215	94.66
SD	0.15	0.35	0.07	0.21	0.021	0.104	0.025	0.05	0.031	0.011	0.11	0.017	0.48
H3-2 ($n = 10$)	5.60	71.66	1.99	3.05	0.054	0.169	0.188	2.54	0.118	0.045	14.50	0.198	96.92
SD	0.16	0.58	0.07	0.07	0.028	0.087	0.016	0.05	0.032	0.011	0.19	0.021	0.50
H3-3 ($n = 9$)	6.01	69.83	2.56	3.23	0.045	0.131	0.235	2.20	0.131	0.047	15.42	0.229	95.50
SD	0.06	0.34	0.06	0.06	0.019	0.056	0.023	0.03	0.027	0.014	0.15	0.017	0.23
H3-5 ($n = 9$)	5.95	70.75	2.43	2.53	0.050	0.144	0.298	2.36	0.153	0.044	15.04	0.329	97.71
SD	0.16	0.34	0.08	0.35	0.027	0.077	0.032	0.03	0.019	0.005	0.13	0.025	0.35
H3-6 ($n = 4$)	5.61	71.93	1.78	3.39	0.034	0.120	0.229	2.70	0.161	0.042	13.77	0.265	98.56
SD	0.14	0.26	0.03	0.24	0.017	0.068	0.022	0.04	0.028	0.003	0.07	0.027	0.11
H3-7 ($n = 5$)	5.24	74.18	1.47	2.08	bd	0.184	0.065	2.90	0.096	0.044	13.64	0.173	97.78
SD	0.35	0.76	0.36	0.13	–	0.099	0.020	0.18	0.024	0.011	0.82	0.017	0.64
H3-8 ($n = 10$)	4.63	72.15	2.43	2.42	0.051	0.176	0.197	2.34	0.112	0.040	15.32	0.225	93.47
SD	0.13	0.40	0.05	0.23	0.025	0.089	0.014	0.05	0.025	0.007	0.12	0.012	0.33
H3-9 ($n = 10$)	3.51	76.90	1.25	1.44	bd	0.166	0.047	2.94	0.077	0.038	13.52	0.141	92.49
SD	0.26	0.54	0.21	0.18	–	0.081	0.024	0.10	0.037	0.006	0.54	0.128	0.48
H3-10 ($n = 10$)	6.31	69.89	2.29	2.83	0.044	0.315	0.233	2.61	0.131	0.045	15.25	0.273	98.65
SD	0.12	0.33	0.05	0.15	0.023	0.195	0.024	0.06	0.036	0.006	0.11	0.028	0.53
H3-11 ($n = 10$)	6.78	71.00	2.44	2.10	0.059	0.152	0.237	2.37	0.108	0.029	15.07	0.276	100.20
SD	0.16	0.42	0.05	0.49	0.032	0.080	0.025	0.03	0.040	0.005	0.12	0.025	0.25
H3-12 ($n = 10$)	5.09	70.46	2.31	3.28	0.046	0.210	0.227	2.60	0.140	0.029	15.40	0.256	95.18
SD	0.24	0.34	0.03	0.19	0.024	0.135	0.027	0.06	0.051	0.010	0.17	0.021	0.38
H3-HR5 ($n = 9$)	3.48	74.31	2.16	2.87	0.014	0.078	0.198	1.66	0.130	0.040	14.88	0.183	93.44
SD	0.17	0.57	0.07	0.38	0.011	0.075	0.024	0.09	0.033	0.008	0.06	0.036	0.68
H3-HR5a-Rev ($n = 10$)	2.60	74.32	2.79	2.14	0.034	0.090	0.146	1.62	0.085	0.022	15.88	0.271	91.48
SD	0.07	0.22	0.08	0.22	0.021	0.064	0.024	0.04	0.037	0.008	0.14	0.013	0.28
H3-HR5b-Rev ($n = 10$)	2.53	73.63	2.69	3.10	0.033	0.088	0.244	1.52	0.125	0.021	15.71	0.307	91.83
SD	0.12	0.25	0.09	0.13	0.012	0.074	0.027	0.06	0.041	0.007	0.17	0.017	0.34
H3-HR6 ($n = 10$)	3.79	77.22	1.23	1.81	0.010	0.112	0.077	2.06	0.101	0.048	13.45	0.088	91.83
SD	0.41	1.13	0.21	0.09	0.007	0.062	0.011	0.13	0.034	0.006	0.56	0.022	0.34

[a] Number of analysis in parentheses.
[b] Total values before normalization to 100% anhydrous.

The phenocryst mineral assemblage in the natural and experimental samples was determined using a combination of optical microscopy and the energy-dispersive x-ray spectroscopy (EDS) system on the electron microprobe or a scanning electron microscope (Zeiss DSM-962). Textural features of mineral phases were recorded by back-scattered electron (BSE) imaging, using a 12 KeV acceleration voltage and magnifications between 100x and 500x. In order to constrain the crystallinity of the natural samples, 10 BSE images were spaced over 6 polished thin sections and the images were analyzed for the area percent of mineral and glass phase using the ImageJ software. The crystallinity of the quenched experimental charges was similarly determined, however only 2–5 BSE images were used due to the smaller amount of material yielded by these experiments.

The bulk-rock major element chemistry of the starting material was analyzed with X-ray fluorescence spectroscopy (XRF), housed at the University of Mainz. Several H3 pumice clasts were powdered using an agate mortar until the material was homogenized. Powdered sample material was mixed with a fluxing agent (Li-tetraborate) and melted at 1050 °C. The resulting glass bead was then analyzed using a Phillips MagiXPRO-XRF. In parallel, the loss on ignition was determined by heating the powder for several hours. XRF analyses were performed on aliquots of the same powdered pumice material used for petrological experiments.

4. Results

4.1. Plagioclase zoning profiles

The zoning patterns of plagioclase phenocrysts are subtle, as evidenced by the crystals' relatively homogeneous appearance in BSE micrographs (Fig. 2). Here we interrogate these textural patterns for indications of magma mixing and thermal effects using high contrast BSE imaging.

Most plagioclase crystals are sub- to euhedral with pronounced faceted rims, suggesting that plagioclase was stable in the magma reservoir prior to eruption. Based on the range of observed textures, 3 sub populations of plagioclase were defined. From these groups, at least one grain of each type was chosen for detailed electron microprobe analysis and BSE imaging. By far, the most common textural category comprises oscillatory zoning throughout the crystal, within a compositional range that almost spans the entire variety of measured An-contents (An_{48-31}). The compositional differences in most grains vary between about 5 and 10 mol% An. Larger zones of about 50 to 100 µm width are assembled of fine oscillatory zones on a smaller scale of ~1 µm.

The second type is distinguished from type 1 only by prominent rounded resorption surfaces surrounding oscillatory-zoned cores (Fig. 2b). The width of resorption zones varies from about 50 to 200 µm, whereby finer growth zones are not ruled out regarding the capability of BSE imaging. The resorption surfaces are marked by an abrupt change in color from grey to black, which is associated with a decrease in the An content of the crystal by about 7 mol%.

Reversed-zoned and partially resorbed cores, that are either homogeneously or patchy-zoned, comprise the third textural type of H3 plagioclase. These crystals consist of a rounded relatively An-poor core (An_{31-35} mol%) that is mantled by more calcic plagioclase showing oscillatory zoning. The increase in An content from core to mantle is the largest observed in all three textural types (~10 mol%). The sample shown in Fig. 2c represents a case in which the calcic composition that is following a potential resorption event gradually evolves back to the values observed in the sodic core.

Discrimination between thermal effects and compositional mixing processes in magma chambers can be achieved using the systematics of anorthite content and FeO_{total} in zoned feldspar crystals (Ginibre et al., 2002). As Fe is not a major element in plagioclase, the partitioning between crystals and melt is controlled by the Fe

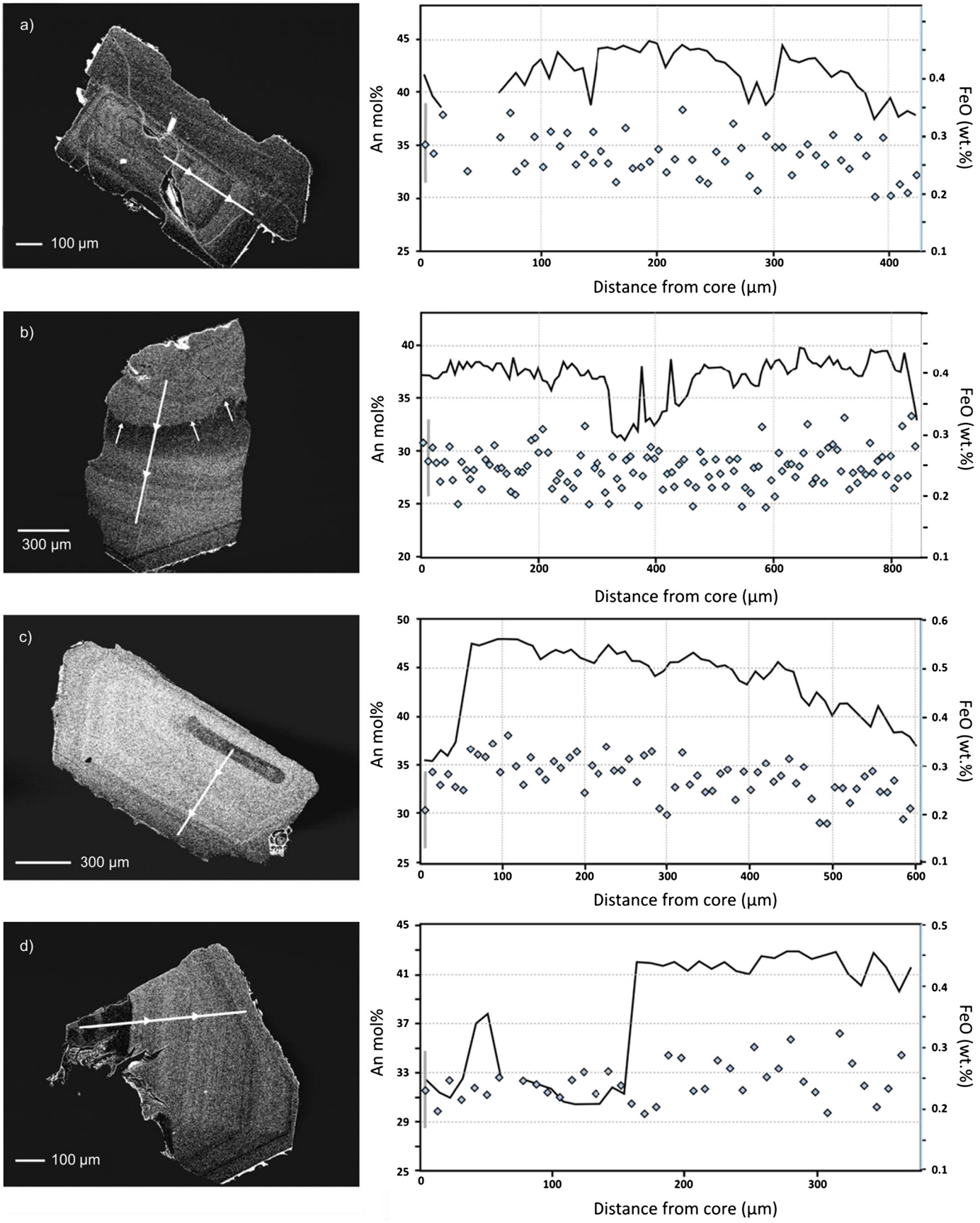

Fig. 2. Back-scatter electron images (left hand side) and high resolution chemical profiles (right hand side) of analyzed H3 plagioclase phenocrysts. The white lines indicate electron microprobe traverses from core to rim of the crystals (arrows indicate direction of analysis). Anorthite contents are represented by a black curve, while FeO_{total} contents are represented by light blue diamonds. 2 sigma error is given. (a) Oscillatory zoned phenocryst. (b) Crystal fragment with resorption zone (marked by arrows) and dark overgrowth texture. (c) Reversely zoned core in oscillatory-zoned crystal. (d) Patchy reversed zoned core and oscillatory overgrowth.

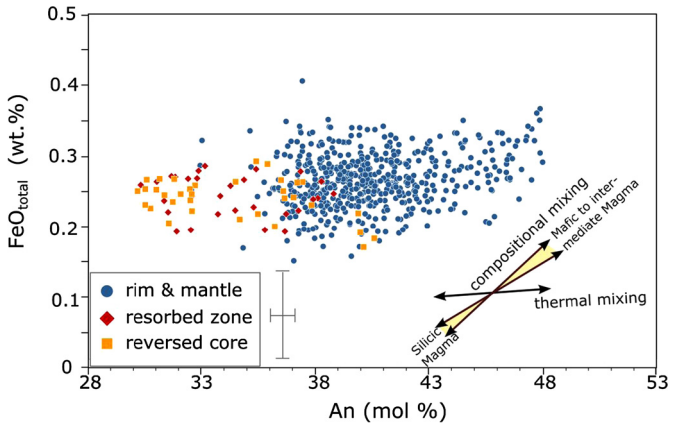

Fig. 3. Bivariate plot of anorthite versus FeO_{total} in H3 plagioclase phenocrysts. Resorption zones and reversed cores are clearly distinguished from rim and mantle composition in terms of their anorthite content. Resorption zones and cores are not significantly different from rim and mantle compositions in terms of their FeO content. Slopes of compositional mixing vectors for mafic to intermediate magmas were determined from average compositions of Icelandic plagioclase crystals ($An_{54–55}$ for basaltic and $An_{66–67}$ for intermediate melts; mined from the GEOROC database), which are representative of Hekla's mafic to intermediate plagioclase. Average An contents of 38 mol% and FeO contents of 0.25 wt.% were chosen as mixing end-member for silicic Hekla magma. The thermal mixing or ascent vector was drawn after Ruprecht and Wörner (2007). 2 sigma error is shown as grey bars.

content of the melt and its oxidation state (Ruprecht and Wörner, 2007). The concentration of FeO_{total} in H3 plagioclase is shown in Fig. 3. Measured FeO_{total} contents vary between 0.36 and 0.14 wt.%, and the variance in individual grains is on the same order as measured in the whole population ($n = 47$ crystals studied). FeO_{total} contents in reversed cores with low anorthite contents are indistinguishable from mantle and rim compositions. This holds also for the concentrations of FeO_{total} after prominent resorption surfaces.

4.2. Experimental results

A total of 24 Co-buffered, H_2O-saturated isobaric and isothermal experiments have been run in the P_{H_2O}–T range of 30 to 200 MPa and 750 to 1030 °C, in order to determine the hydrous phase equilibria for Hekla's H3 rhyodacite. Table 2 provides an overview of the intensive variables in each experiment, the run duration, and crystallinity, which was determined from 2D SEM-BSE image analysis, and the observed phase assemblage of the experimental run products. Evidence that equilibrium conditions were reached in most experiments comprises euhedral and subhedral crystal habits, spatially homogeneous groundmass glass compositions, and systematic changes of crystallinity under de- or increasing temperature and P_{H_2O}, confirming that the reaction kinetics were on the same timescale as the experiments.

The natural Hekla H3 phenocryst assemblage, along with glass and vesicles, which are present in all experimental run products, has been reproduced by 9 petrological experiments (Table 2: H3-2, H3-3, H3-6, H3-8, H3-9, H3-20, H3-21, HR-6, HR-5a; Fig. 6). Of the 9 experiments, only two experiments (Table 2: H3-3, H3-8) had crystal volume percentages matching the natural pumice of 2 to 11 vol.% (Sverrisdottir, 2007). However, experiment H3-3 (850 °C, 200 MPa) is near the limit of the plagioclase stability field and fayalitic olivine becomes the dominant mineral phase.

The major element chemistry of experimental glasses is compared to the natural matrix glass compositions in Fig. 4. The isothermal sequence at 850 °C is of special interest, since it permits evaluating the influence of P_{H_2O} on glass chemistry at a temperature in the range inferred from Fe–Ti oxide thermometry and plagioclase–melt hygrometry for H3 rhyodacite (835–865 °C; Waters and Lange, 2015; Portnyagin et al., 2012). Experiments in the P_{H_2O} range of 100 and 150 MPa best match the major element chemistry of the natural H3 matrix glass. Experimental crystallinity values replicate the nearly aphyric character of the H3 rhyodacite at 150 MPa.

A comparison between natural and experimental plagioclase compositions is shown in Fig. 5a. Both natural and experimental plagioclase plots in a narrow range within the andesine field between 30 and 48 mol% anorthite. However, a wide range of experimental conditions produce the natural compositions. The plagioclase crystals in our experimental run products are euhedral to subhedral and do not show features that would be expected for entrained crystals from the original starting material.

The natural pyroxenes are Ca-rich augite, with a mean composition of $Wo_{41}En_{20}Fs_{40}$, which is a close match to the experimental mean composition of $Wo_{41}En_{21}F_{s38}$ (Fig. 5b). Experimental augite variability also reproduces the natural range of observed endmember compositions. No clear systematic dependence between experimental run conditions and clinopyroxene composition could be found. However, low-pressure experiments tend to have higher enstatite contents compared to high pressure ones.

Experimental olivine major element compositions very closely match the natural compositional variability observed in H3 olivine, which ranges between 83 and 84 mol% fayalite component. Again, no systematic dependence of olivine Fa-content on experimental intensive variables is evident. Nickel-buffered experiments on the Hekla H3 rhyodacite, incidentally do not permit new fayalite growth but rather cause magnetite-rich reaction rims to grow on olivine grains due to relatively more oxidizing conditions (Supplementary Fig. 1).

5. Discussion

5.1. Shallow magma storage conditions of silicic Icelandic magmas

Fig. 6 summarizes the experimental results in a phase equilibria diagram for H_2O-saturated Hekla 3 rhyodacite. We reiterate that only the 850 °C experiments between 100 and 150 MPa reproduce the mineral assemblage (pl > ol + cpx > ilm + mt > ap + zrc), matrix glass chemistry and natural crystallinity within the considered experimental range; these experiments define the most likely pre-eruptive storage conditions. Taken together, the H_2O-saturated phase equilibria experiments are indicative of rather restricted pre-eruptive magma storage conditions: P_{H_2O} from 130 to 175 MPa and temperatures of around 850 °C. H_2O-saturation at these pressures implies that the melt would have contained between 4 and 5.4 wt.% dissolved H_2O (Newman and Lowenstern, 2002). The pressure values translate to relatively shallow crustal depths of just 5 to 6.6 km, assuming average crustal density of 2.7 kg/cm^3 (Darbyshire et al., 2000). We emphasize that the occurrence of fayalitic olivine and the lack of amphibole in silicic Hekla magmas, as well as in our experiments, most likely indicates the low oxidation state of the magma, as this fosters relatively high amounts of ferrous iron (Fe^{2+}) in the melt (e.g., Carmichael, 1991; Portnyagin et al., 2012; Scaillet et al., 2016; Supplementary Information).

Experimentally determined storage parameters (Fig. 6) are consistent with the results of Portnyagin et al. (2012), who constrained crystallization temperatures based on olivine–melt equilibria (855 °C to 901 °C; Putirka, 2008) and coexisting ilmenite-magnetite pairs (840 °C to 940 °C), in addition to water concentrations in olivine-hosted H3 melt inclusions. The most evolved H3 melt inclusions, which are compositionally similar to the H3 groundmass glass, yielded crystallization temperatures at the lower end of this range (840–865 °C), which is a good match to the experimentally determined temperature (850 °C). Application of

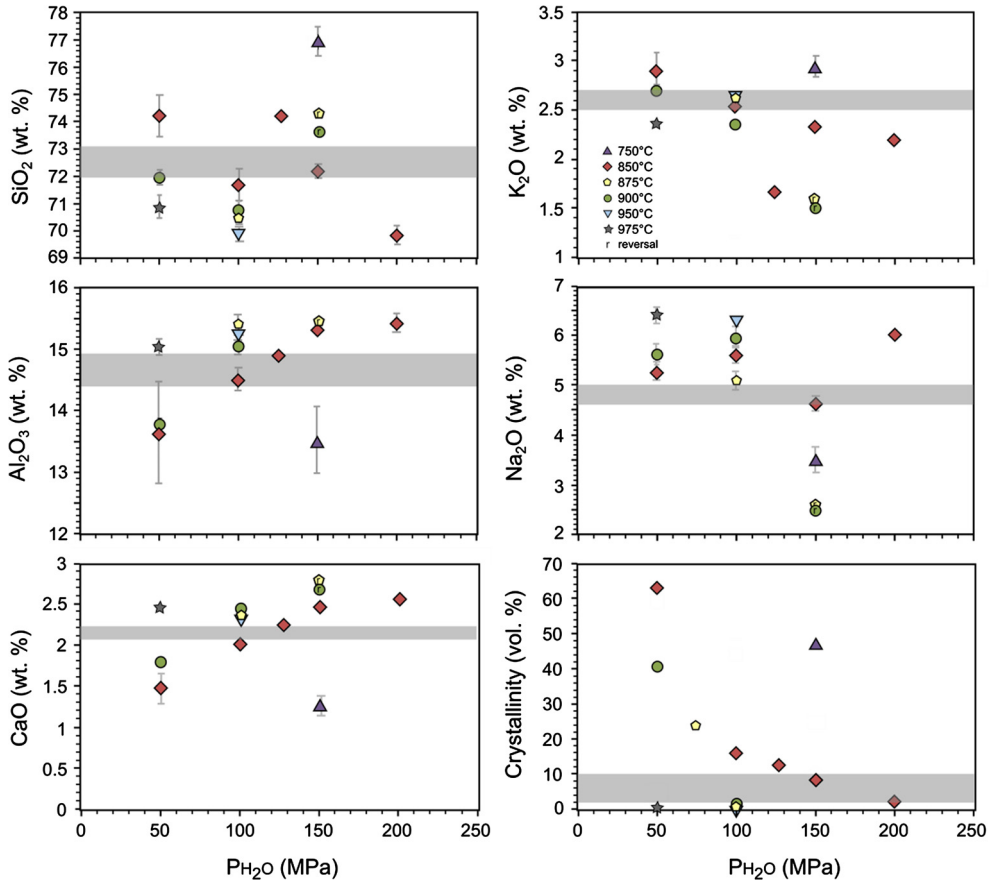

Fig. 4. Comparison of natural glass chemistry and crystallinity (grey horizontal bars) with experimentally generated glasses under varying P_{H_2O} and temperatures. The 1-sigma standard deviations about the mean value are shown for natural and experimental data. All glass data were normalized to 100% anhydrous. The closest match between natural and experimental glass compositions, as well as crystallinity values is obtained for experiments at 850 °C and in the P_{H_2O} range between 100 and 150 MPa.

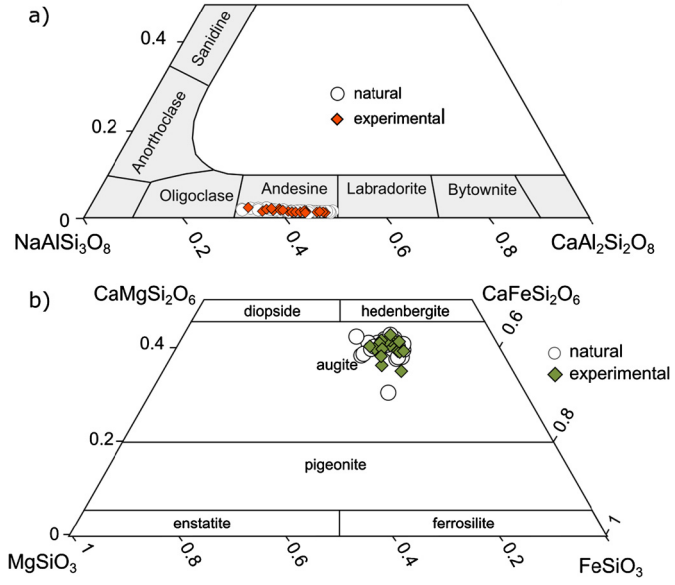

Fig. 5. Chemical compositions of natural (open circles) and experimental (diamonds) plagioclase (a) and pyroxenes (b). Experimental mineral chemistries are all grouped together since no systematic dependence of the P_{H_2O} sequence at 850 °C on plagioclase or pyroxene composition was observable in the data.

a plagioclase–melt hygrometer on Hekla H3 equilibrium plagioclase (An_{38}) and groundmass glass composition (Waters and Lange, 2015) yields a temperature of 835 °C for the highest observed H_2O content in H3 melt inclusions (Supplementary Fig. S2).

Olivine-hosted melt inclusions analyzed by Portnyagin et al. (2012) and Lucic et al. (2016) preserve water contents up to 5.41 wt.% and 5.67 wt.% for the H3 magma respectively, consistent with a narrow range of pressures (at 835–865 °C are 185–189 MPa; Newman and Lowenstern, 2002). A maximum value of 6.15 wt.% H_2O (209 MPa at 835 °C; Newman and Lowenstern, 2002) has been obtained for the rhyolitic H4 magma (Portnyagin et al., 2012), which was erupted approximately 1000 years before H3. Our experimentally determined storage pressures at P_{H_2O} up to 175 MPa are slightly lower than these entrapment pressures, but are based on many experimentally constrained mineralogical and glass compositional indices within the whole phenocryst assemblage. Melt inclusion entrapment pressures are, by contrast, relevant to the specific host crystal's nucleation and growth history, so some offset between crystal-host and phenocryst-assemblage-based inferred pressures is to be expected. For example, Portnyagin et al. (2012) found a positive correlation between H_2O and K_2O in silicic and more mafic Hekla olivine hosted melt inclusions, suggesting entrapment during progressive H_2O undersaturated crystallization. Such a correlation is not apparent from the data presented in Lucic et al. (2016), potentially due to loss of H_2O during degassing. Our results show, however, that olivine is stable at 200 MPa and temperatures <880 °C, thus indicating that entrapment of melt inclusions could have occurred at higher pressures before these phenocrysts were transported to a final, shallower storage depth. This model requires that extensive differentiation happens at greater depth—potentially within a mafic parent magma—than the final storage prior to eruption, and is in line with production of silicic magmas in deep crustal hot zones (Annen et al., 2006).

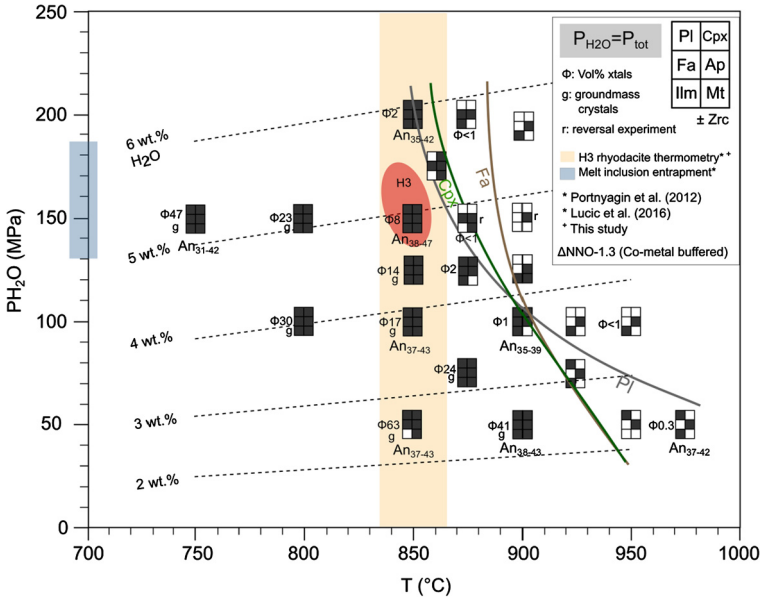

Fig. 6. Experimental P_{H_2O}–T phase diagram for H_2O saturated Hekla rhyodacite. The box symbols represent fixed P_{H_2O}–T experiments under H_2O saturated conditions. Small sub-squares show the mineral phases that are present in the quenched experimental products. Approximate phase boundaries are shown for plagioclase, clinopyroxene and fayalite by curved mineral-in lines. Dashed lines represent calculated water concentration in saturated rhyolitic melt using VolatileCalc on a CO_2 free basis (Newman and Lowenstern, 2002). The yellow bar represents thermometry data for H3 melt inclusions similar in composition to the H3 groundmass glass (Portnyagin et al., 2012), as well as temperatures calculated using the plagioclase–melt thermometer from Waters and Lange (2015). A red ellipse marks the best fit between melt inclusion entrapment pressure, geothermometry, phase stability, mineral chemistry and crystallinity.

The pressure corresponding to H_2O contents of 5.67 wt.% was calculated on a CO_2-free basis using the algorithm of Newman and Lowenstern (2002). If we would assume that the natural mineral assemblage crystallized in the presence of a mixed H_2O–CO_2 fluid, this would imply H_2O-undersaturated mineral growth at higher temperature and/or pressures than our experimental magma storage conditions indicate. CO_2 concentrations in evolved Hekla magmas are, however, generally very low <20–30 ppm (Lucic et al., 2016). Thus, if these melt inclusion data represent primary CO_2 concentrations then our magma storage estimates are reliable and do not need significant adjustments to account for the presence of a mixed fluid phase.

We test how Hekla's shallow silicic reservoir may have been subjected to thermal and perhaps compositional eruption triggering, by interrogating chemical zoning in plagioclase. Chemical zoning of natural H3 plagioclase phenocrysts records changes in backscattered electron intensity (Fig. 2), which correlates to intracrystal variations in An content of up to 10 mol%. The rounded resorption surfaces observed both on low-An cores and within crystals (Fig. 2b, c) likely reflect thermal perturbations in the resident magma body potentially caused by magma under-plating or mingling. Following periods of plagioclase dissolution, the crystals apparently grew higher-An content overgrowths in response to hotter melt temperature. In some cases (e.g., type 3 plagioclase; Fig. 2c) the compositions of overgrowths migrated back towards pre-resorption values. A gradual decrease in An content with time (Fig. 2c) is expected from progressive crystallization down a temperature gradient, or due to loss of H_2O from the system. The relatively narrow range of variation in An-content with FeO (Fig. 3) is consistent with crystallization within a magma reservoir that was undisturbed by compositional mixing events with less-evolved melt. Hence, it is very likely that these plagioclase phenocrysts grew from a compositionally homogeneous melt. The subtle variation seen in An content and FeO is best explained by progressive but perhaps not extensive crystallization in a magma body, where local thermal and/or P_{H_2O} heterogeneities modify the chemical composition of the plagioclase.

Finally, it is interesting to note that several of Hekla's Holocene silicic eruptions produced a common and identical phase assemblage to the H3: plagioclase, clinopyroxene, fayalitic olivine and titanomagnetite (Larsen and Thorarinsson, 1977; Sverrisdottir, 2007; Meara, 2012). These similar mineralogical and geochemical features may indicate that the shallow storage depths inferred from experimental phase petrology (Fig. 6) could be representative of a periodically replenished silicic reservoir feeding large dacitic to rhyolitic eruptions at Hekla.

5.2. Magmatic architecture and implications for pre-eruptive deformation

A number of studies (Soosalu and Einarsson, 2004; Ofeigsson et al., 2011; Geirsson et al., 2012; Sturkell et al., 2013) have shown that modern day eruptions of basaltic andesite magmas from Hekla volcano are fed from a relatively deep storage, between 10 and 25 km in the Icelandic crust. Our experimental results, along with geothermobarometric studies (Portnyagin et al., 2012) reveal that Hekla also stores shallow H_2O-rich silicic magma and is therefore best characterized by poly-baric magma architecture.

This shallow silicic storage region is probably not disturbed by large-scale compositional mixing events or magma chamber overturn, as prominent resorption surfaces with Ca- and Fe-rich overgrowth are sparse within the plagioclase population. Minor recharge with basaltic andesite magma into the silicic complex is yet likely, as Hekla eruption deposits are chemically zoned indicating more mafic material erupting after silicic magma. Some crystals show An contents in reversed cores that are low enough to be in equilibrium with a melt with higher SiO_2 concentration than the most evolved H3 magma, showing that some crystal cores from previous silicic episodes may have been recycled.

The deformation patterns observed from geodetic monitoring at Hekla are linked to the deflation or inflation of the lower crustal storage zone and therefore the magmatic architecture of the system. No geophysical evidence for accumulation of magmatic liquids in the shallow crust beneath Hekla has so far been found

(Soosalu and Einarsson, 2004). Thus, intrusion of evolved magmas either from a deep crustal hot zone (Annen et al., 2006), or the reactivation of a shallow resident silicic crystal mush e.g. by mafic dyke injection, would be required to accumulate eruptible silicic magma at depths consistent with experimentally constrained reservoir limits (Jay et al., 2014).

As the constrained pre-eruptive storage conditions for the Hekla rhyodacite are very different from the currently inferred deep crustal storage zone, we anticipate that future eruptions of silicic magma from Hekla may be preceded by surface deformation patterns that differ from modern day observations, which are related to the deep mafic storage zone. More specifically, the contemporary area of broad crustal deformation surrounding Hekla, with a radius of about 20 km around the volcano (Ofeigsson et al., 2011), would probably be narrower (e.g., Muir et al., 2014).

In order to evaluate how surface deformation prior to silicic eruptions might differ from the deformation signals obtained from the more recent smaller events, we use finite-element modeling of surface displacement, in which the stress and strain resulting from a pressure boundary load is numerically solved. The crust beneath Hekla volcano is modeled in 2D-axisymmetrical space using COMSOL Multiphysics v5.2a (Fig. 7; Supplementary Table S1), in which surface displacement results from the pressurization of two stacked cavities so as to simulate the possible deep mafic and shallow silicic reservoirs under the volcano. We test two different magma storage geometries for the deeper of the two magma

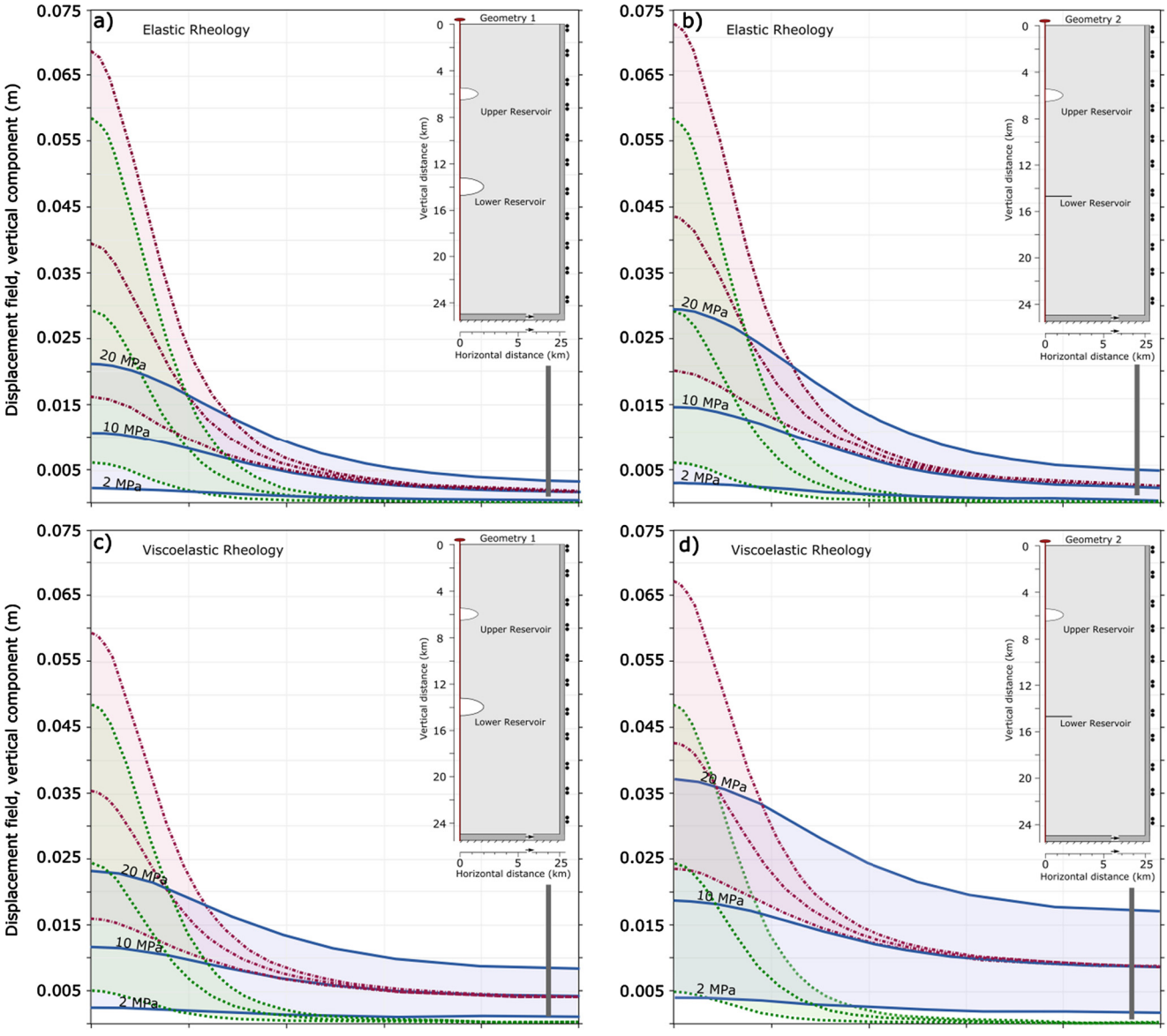

Fig. 7. Calculated vertical (a–d) and horizontal (e–f) displacement at the Earth's surface versus horizontal distance from the surface centerline. Insets in figures a) and b) show the setup used for finite element modeling: Both geometries are implemented in 2D-axisymmetrical space with 25 km horizontal and vertical distance from the center, surrounded by an infinite element domain. A roller condition and fixed constraint are applied to the vertical and lower horizontal boundary, respectively. The surface is free to deform in the modeling setup. Pressurization of a lower or upper magma reservoir is employed by a boundary load of 2, 10 or 20 MPa (Gudmundsson, 2016) on reservoir surfaces. The two modeling geometries differ only in the dimensions of the lower chamber (see insets), which is represented by an oblate ellipsoid in geometry 1 and as a sill in geometry 2 (horizontal black line). Dashed curves with pressure labels (exemplary shown for the solid blue lines) represent pressurization of either the lower reservoir (blue – solid), upper reservoir (green – dotted) or both inflation sources (red – dash–dot). Models in both geometries have been run with elastic rheology (Fig. 7a, b) as well as viscoelastic rheology (Fig. 7c, d). Horizontal surface displacement results are shown on figures e) and f). Vertical grey bars in each plot represent typical errors for GPS displacement measurements (Sigmundsson et al., 2010). The modeling was carried out in COMSOL Multiphysics version 5.2.

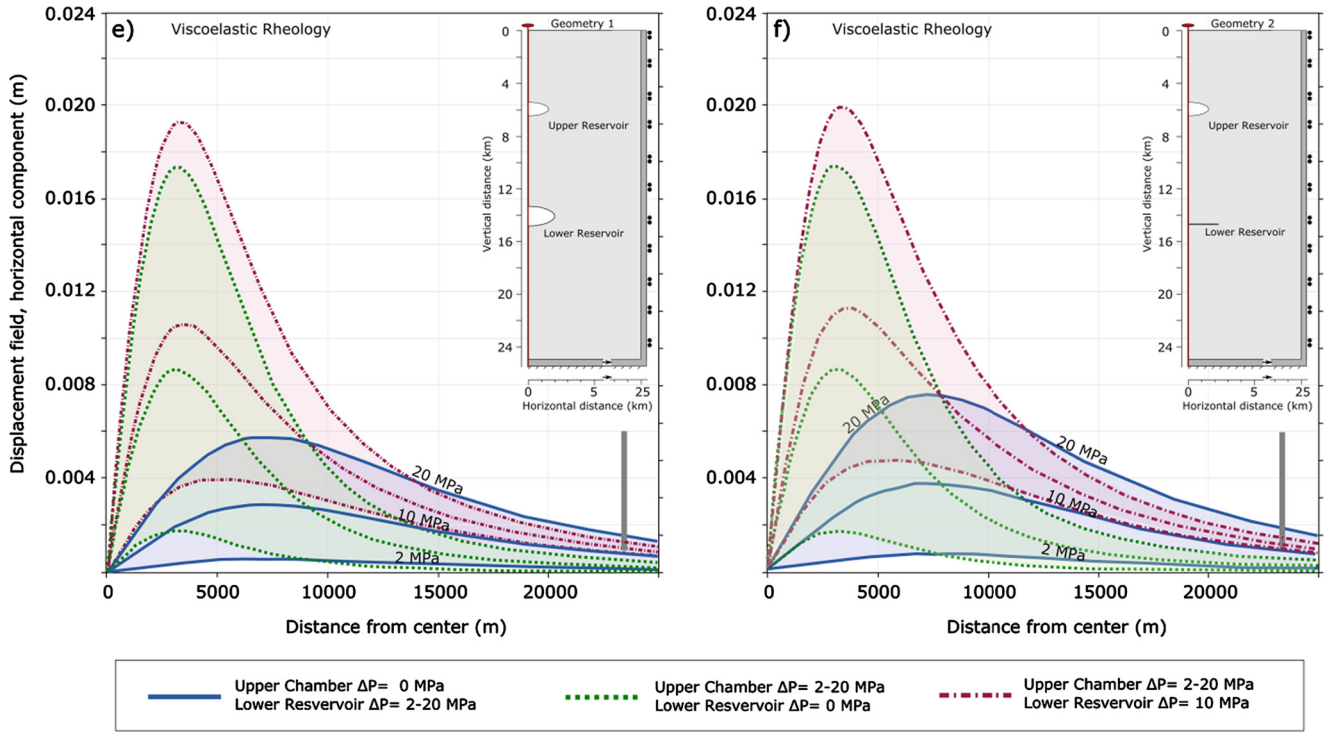

Fig. 7. (*continued*)

bodies. In Geometry 1, the reservoir is modeled as an oblate ellipsoid, similar to that investigated by Ofeigsson et al. (2011), who modeled the present day surface deformation at Hekla as resulting from a spherical source between 14 and 16 km depth. The surface displacement at Hekla can, however, also be fit with an axisymmetric sill geometry at 14.8 km depth with radius of 4.5 km and thickness of 3 m (Grapethin et al., 2010), which defines our second modeling geometry.

We implemented a depth dependent density structure based on Darbyshire et al. (2000) and crustal Young's modulus heterogeneity calculated using the density profile and P-wave seismic velocities from Tryggvason et al. (2002; Supplementary Fig. S3). Further, models with elastic and viscoelastic rheology were run and compared. In viscoelastic models crustal heterogeneity is implemented via depth-dependent Bulk (K) and Shear (G) Modulus (Supplementary Table S1). As viscous creep introduces a time dependency in such models, we simulated source pressurization for 3 month with monthly time-steps. These temporal considerations are based on results obtained for pre-eruptive magma recharge from diffusion chronometry (Morgan et al., 2004) and from the timing of volcanic unrest expressed as precursory geophysical signals (Sigmundsson et al., 2010). Like in the elastic modeling setup, the source pressure was taken to be constant in viscoelastic runs. Both elastic and viscoelastic modeling setups were benchmarked against analytical solutions of surface deformation before adding further complexity (i.e., stacked magma reservoirs, crustal heterogeneity). All simulations were run using >29900 triangular mesh elements and compare well to the benchmarking results presented by Hickey and Gottsmann (2014) with a misfit of less than 1 mm between numerical and analytical solutions.

Clearly, as illustrated in Fig. 7, the shallower storage depth results in a narrower displacement curve (i.e., surface deformation) as a function of the distance from inflation source, whereas the deeper reservoir produces a broad area of deformation around the center (Dzurisin, 2006). This is consistent with geodetic observations for basaltic andesite eruptions (Ofeigsson et al., 2011; Geirsson et al., 2012; Sturkell et al., 2013) and petrogenetic considerations (Höskuldsson et al., 2007) at Hekla volcano. The relative difference between narrow surface deformation stemming from an upper reservoir and a broad signal from a deeper magma source is more pronounced in modeling setups with viscoelastic rheology (Fig. 7c and 7d) compared to elastic runs (Fig. 7a and 7b; Del Negro et al., 2009). Further, pressurization of a deep sill-shaped reservoir (Fig. 7b and 7d) would favor a larger relative difference (Dzurisin, 2006).

The maximum amplitudes of our predicted vertical surface displacements are on the order of 2–36 mm for the deep source, while shallow reservoir pressurization results in displacements of about 5–60 mm above the inflation center. In the case where both sources would be active, a maximum vertical movement of 73 mm is predicted by our models (Fig. 7). Using InSAR data, Jay et al. (2014) successfully detected surface uplift of 60 mm in an observation window of 3 months before the shallowly sourced eruption of Cordón Caulle in 2011. Pre-eruptive deformation can also be tracked by GPS with a precision of 20 mm in vertical displacement and ∼5 mm in the horizontal component, as demonstrated for the 2010 Eyjafjallajökull eruption (Sigmundsson et al., 2010). Comparing these data to our modeling outputs shows that InSAR and GPS could potentially be valuable techniques to identify reactivation of Hekla's shallow silicic reservoir. Our results are certainly within the resolution of these methods under the following "ideal" conditions: 1) high overpressures (∼20 MPa) in the shallow source or 2) combined shallow pressurization with background deformation signals arising from the deep source (Fig. 7). However, considering that the amplitudes of surface deformation are highly dependent on modeling variables like the size and geometry of the pressurized source, we caution that smaller upper-crustal inflation sources than the ∼4.7 km^3 oblate ellipsoid used in our modeling setup might be difficult to detect.

In order to test if focused narrow vertical displacement resulting from pressurization of a shallow source could be masked by simultaneous inflation of the deeper reservoir, we ran simulations for a range of excess pressure values (2 MPa, 10 MPa and 20 MPa) in both magma reservoirs (Gudmundsson, 2016). Our results indi-

cate that when both reservoirs are pressurized, the resulting signal will consist of a broad area of deformation around the inflation source, paired with a narrower curve around the center (Fig. 7; Supplementary Fig. S4). This effect is also pronounced for relatively low ΔP in the upper reservoir (e.g. 2 MPa), while having a comparatively high excess pressure of 10 MPa in the lower reservoir (cf. red-dashed–dot curves in Fig. 7). For such a scenario, that is the pressurization and failure of a deeper source and subsequent injection of the mobilized magma into a shallower reservoir, our modeling shows that signals emerging from the shallow pressurization could potentially be discriminated from broader, deeply sourced magmatic processes. As illustrated in Fig. 7d, large excess pressures of 20 MPa in the shallow source and simultaneous pressurization of the lower reservoir with 10 MPa results in ~48 mm more vertical uplift than a single deep pressure source at 10 MPa. Furthermore, the lateral extent of the combined deformation signal is more restricted than a deep source alone and rapidly decays with distance from the inflation center. However, as shown in Fig. 7e–f, even though the maximum difference of 17 mm in horizontal displacement is smaller compared to vertical uplift, the higher resolution of horizontal-component GPS measurements could help discriminate between deformation sources.

Local irregular topography has been shown to be an influencing factor when trying to fit surface displacement patterns due to surface strain localization (Hickey et al., 2016). As we are not trying to fit a specific deformation signal, but explore different magma storage and surface displacement scenarios, we do not consider topographic heterogeneity in our models. Temperature-dependence included within mechanical modeling has also been shown to effect surface deformation results, due to the temperature dependency of viscosity (Hickey and Gottsmann, 2014). Implementation of a temperature-dependent viscoelasticity could result in higher vertical displacement as predicted by our models, even though this effect is highly dependent on the model setup (Hickey and Gottsmann, 2014; Gregg et al., 2012).

We conclude that an imminent silicic eruption from Hekla volcano could be foreseen by sharper, more focused surface deformation stemming from a shallow silicic magma storage region. Such an effect could potentially also be seen if there was simultaneous pressurization of the lower crustal magma storage zone. The possibility of a silicic eruption sourced from the deeper source is possible but unlikely, since all recent silicic Hekla magmas share common mineralogical and petrological characteristics that point to shallow storage <7 km depth (Sigmarsson et al., 1992, Sverrisdottir, 2007; Meara, 2012). Eruption triggering by injection of more mafic material has been shown to be an important process in Icelandic volcanism in general (Sparks and Sigurdsson, 1977; Sverrisdottir, 2007; Sigmarsson et al., 2011), which in theory should produce changes in volume and pressure and therefore surface deformation signals, as was the case for the 2011–2012 rhyolite eruption of Cordón Caulle (Jay et al., 2014). The timescale on which Hekla is capable of accumulating eruptible silicic magma batches and the longevity of such reservoirs in the crust are currently unknown and could be a target for future studies.

6. Conclusions

Experimental petrological constraints on magma storage prior to Hekla's H3 Plinian eruption reveal distinctly shallower conditions than previously inferred for mafic eruptives at Hekla. Natural rhyodacite pumice mineral and glass chemistry from the H3 eruption were experimentally reproduced under H_2O-saturated conditions, and with ~ΔNNO-1.3 at a temperature of 850 °C and H_2O pressure of 130 to 175 MPa, implying magma storage depths of just 5 to 6.6 km beneath the volcano. These results are consistent with geothermobarometric data derived from melt inclusions and plagioclase–melt thermometry and provide a robust petrological estimate of magma storage prior to silicic Hekla eruptions. Chemical zoning patterns of plagioclase phenocrysts show that magma mixing did not disturb the silicic reservoir. Instead, local thermal or volatile gradients affected the plagioclase population within the reservoir. We conclude that future large silicic eruptions from Hekla volcano could be fed from an upper crustal reservoir with pre-eruptive conditions similar to those obtained in this study. Forward deformation modeling of these storage conditions suggests that future injections of silicic magma to the shallow reservoir could generate surface deformation that is characterized by narrower yet significant uplift and therefore discriminible from currently observed broad deformation attributed to deep mafic magma storage. Our combination of experimental phase petrology with forward deformation modeling represents a fruitful avenue to forecast pre-eruptive unrest at active and restless volcanoes.

Acknowledgements

We would like to thank S. Buhre and N. Groschopf for their helpful analytical support. Financial support from the VAMOS research centre at the Johannes Gutenberg University is kindly acknowledged. We highly appreciate the comments by the editor Tamsin Mather and reviewer James Hickey, as well as two anonymous reviewers on earlier versions of the manuscript, that helped to improve it significantly.

Appendix A. Supplementary material

Supplementary material related to this article can be found online at http://dx.doi.org/10.1016/j.epsl.2017.03.015.

References

Annen, C., Blundy, J.D., Sparks, R.S.J., 2006. The genesis of intermediate and silicic magmas in deep crustal hot zones. J. Petrol. 47 (3), 505–539.
Barker, S.J., Wilson, C.J., Morgan, D.J., Rowland, J.V., 2016. Rapid priming, accumulation, and recharge of magma driving recent eruptions at a hyperactive caldera volcano. Geology 44 (4), 323–326.
Caricchi, L., Biggs, J., Annen, C., Ebmeier, S., 2014. The influence of cooling, crystallisation and re-melting on the interpretation of geodetic signals in volcanic systems. Earth Planet. Sci. Lett. 388, 166–174.
Carmichael, I.S., 1991. The redox states of basic and silicic magmas: a reflection of their source regions? Contrib. Mineral. Petrol. 106 (2), 129–141.
Castro, J.M., Dingwell, D.B., 2009. Rapid ascent of rhyolitic magma at Chaitén volcano, Chile. Nature 461, 780–783.
Castro, J.M., Schipper, C.I., Mueller, S.P., Militzer, A.S., Amigo, A., Parejas, C.S., Jacob, D., 2013. Storage and eruption of near-liquidus rhyolite magma at Cordón Caulle, Chile. Bull. Volcanol. 75 (4), 1–17.
Castro, J.M., Cordonnier, B., Schipper, C.I., Tuffen, H., Baumann, S.P., Feisel, Y., 2016. Rapid laccolith intrusion driven by explosive volcanic eruption. Nat. Commun. 7 (13585). http://dx.doi.org/10.1038/ncomms13585.
Darbyshire, F.A., White, R.S., Priestley, K.F., 2000. Structure of the crust and uppermost mantle of Iceland from a combined seismic and gravity study. Earth Planet. Sci. Lett. 181 (3), 409–428.
Del Negro, C., Currenti, G., Scandura, D., 2009. Temperature-dependent viscoelastic modeling of ground deformation: application to Etna volcano during the 1993–1997 inflation period. Phys. Earth Planet. Inter. 172 (3), 299–309.
Devine, J.D., Gardner, J.E., Brack, H.P., Laynet, G.D., Rutherford, M.J., 1995. Comparison of microanalytical methods for estimating H_2O contents of silicic volcanic glasses. Am. Mineral. 80 (3–4), 319–328.
Dugmore, A.J., Cook, G.T., Shore, J.S., Newton, A.J., Edwards, K.J., Larsen, G., 1995. Radiocarbon dating tephra layers in Britain and Iceland. Radiocarbon 37 (2), 379–388.
Dzurisin, D., 2006. Volcano Deformation: New Geodetic Monitoring Techniques. Springer Science & Business Media.
Geirsson, H., LaFemina, P., Árnadóttir, T., Sturkell, E., Sigmundsson, F., Travis, M., Bennett, R., 2012. Volcano deformation at active plate boundaries: deep magma accumulation at Hekla volcano and plate boundary deformation in south Iceland. J. Geophys. Res., Solid Earth 117 (B11).
Ginibre, C., Wörner, G., Kronz, A., 2002. Minor- and trace-element zoning in plagioclase: implications for magma chamber processes at Parinacota volcano, Northern Chile. Contrib. Mineral. Petrol. 143 (3), 300–315.

Grapenthin, R., Ófeigsson, B.G., Sigmundsson, F., Sturkell, E., Hooper, A., 2010. Pressure sources versus surface loads: analyzing volcano deformation signal composition with an application to Hekla volcano, Iceland. Geophys. Res. Lett. 37 (20).

Gregg, P.M., De Silva, S.L., Grosfils, E.B., Parmigiani, J.P., 2012. Catastrophic caldera-forming eruptions: thermomechanics and implications for eruption triggering and maximum caldera dimensions on Earth. J. Volcanol. Geotherm. Res. 241, 1–12.

Gudmundsson, A., 2016. The mechanics of large volcanic eruptions. Earth-Sci. Rev. 163, 72–93.

Harlow, D.H., Power, J.A., Laguerta, E.P., Ambubuyog, G., White, R.A., Hoblitt, R.P., 1996. Precursory seismicity and forecasting of the June 15, 1991, eruption of Mount Pinatubo. In: Fire and Mud: Eruptions and Lahars of Mount Pinatubo, Philippines, pp. 223–247.

Hickey, J., Gottsmann, J., 2014. Benchmarking and developing numerical Finite Element models of volcanic deformation. J. Volcanol. Geotherm. Res. 280, 126–130.

Hickey, J., Gottsmann, J., Nakamichi, H., Iguchi, M., 2016. Thermomechanical controls on magma supply and volcanic deformation: application to Aira caldera, Japan. Sci. Rep. 6, 32691.

Höskuldsson, Á., Óskarsson, N., Pedersen, R., Grönvold, K., Vogfjörð, K., Ólafsdóttir, R., 2007. The millennium eruption of Hekla in February 2000. Bull. Volcanol. 70 (2), 169–182.

Jay, J., Costa, F., Pritchard, M., Lara, L., Singer, B., Herrin, J., 2014. Locating magma reservoirs using InSAR and petrology before and during the 2011–2012 Cordón Caulle silicic eruption. Earth Planet. Sci. Lett. 395, 254–266.

Jónasson, K., 2007. Silicic volcanism in Iceland: composition and distribution within the active volcanic zones. J. Geodyn. 43 (1), 101–117.

Kjartansson, E., Gronvold, K., 1983. Location of a magma reservoir beneath Hekla volcano, Iceland. Nature 301, 139–141.

Larsen, G., Thorarinsson, S., 1977. H4 and other acid Hekla thepra layers. Jökull 27, 1–19.

Linde, A.T., Agustsson, K., Sacks, I.S., Stefansson, R., 1993. Mechanism of the 1991 eruption of Hekla from continuous borehole strain monitoring. Nature 365 (6448), 737–740.

Lipman, P.W., Mullineaux, D.R. (Eds.), 1981. The 1980 Eruptions of Mount St. Helens. US Dept. of the Interior, US Geological Survey, Washington, No. 1250.

Lucic, G., Berg, A.S., Stix, J., 2016. Water-rich and volatile-undersaturated magmas at Hekla volcano, Iceland. Geochem. Geophys. Geosyst. 17 (8), 3111–3130.

Matthews, W., Linnen, R.L., Guo, Q., 2003. A filler-rod technique for controlling redox conditions in cold-seal pressure vessels. Am. Mineral. 88 (4), 701–707.

Meara, R.H., 2012. Geochemical Fingerprinting of Icelandic Silicic Holocene Tephra Layers. PhD Thesis. University of Edinburgh.

Morgan, D.J., Blake, S., Rogers, N.W., DeVivo, B., Rolandi, G., Macdonald, R., Hawkesworth, C.J., 2004. Time scales of crystal residence and magma chamber volume from modelling of diffusion profiles in phenocrysts: Vesuvius 1944. Earth Planet. Sci. Lett. 222 (3), 933–946.

Muir, D.D., Blundy, J.D., Rust, A.C., Hickey, J., 2014. Experimental constraints on dacite pre-eruptive magma storage conditions beneath Uturuncu volcano. J. Petrol. 55 (4), 749–767.

Newman, S., Lowenstern, J.B., 2002. VolatileCalc: a silicate melt–H_2O–CO_2 solution model written in Visual Basic for Excel. Comput. Geosci. 28 (5), 597–604.

Ofeigsson, B.G., Hooper, A., Sigmundsson, F., Sturkell, E., Grapenthin, R., 2011. Deep magma storage at Hekla volcano, Iceland, revealed by InSAR time series analysis. J. Geophys. Res., Solid Earth 116 (B5).

Parks, M.M., Biggs, J., England, P., Mather, T.A., Nomikou, P., Palamartchouk, K., Papanikolaou, X., Paradissis, D., Parsons, B., Pyle, D.M., Raptakis, C., Zacharis, V., 2012. Evolution of Santorini Volcano dominated by episodic and rapid fluxes of melt from depth. Nat. Geosci. 5, 749–754.

Pichavant, M., Costa, F., Burgisser, A., Scaillet, B., Martel, C., Poussineau, S., 2007. Equilibration scales in silicic to intermediate magmas—implications for experimental studies. J. Petrol. 48 (10), 1955–1972.

Portnyagin, M., Hoernle, K., Storm, S., Mironov, N., van den Bogaard, C., Botcharnikov, R., 2012. H_2O-rich melt inclusions in fayalitic olivine from Hekla volcano: implications for phase relationships in silicic systems and driving forces of explosive volcanism on Iceland. Earth Planet. Sci. Lett. 357, 337–346.

Putirka, K.D., 2008. Thermometers and barometers for volcanic systems. Rev. Mineral. Geochem. 69 (1), 61–120.

Ruprecht, P., Wörner, G., 2007. Variable regimes in magma systems documented in plagioclase zoning patterns: El Misti stratovolcano and Andahua monogenetic cones. J. Volcanol. Geotherm. Res. 165 (3), 142–162.

Rutherford, M.J., Sigurdsson, H., Carey, S., Davis, A., 1985. The May 18, 1980, Eruption of Mount St. Helens 1. Melt composition and experimental phase equilibria. J. Geophys. Res. 90, 2929–2947.

Scaillet, B., Holtz, F., Pichavant, M., 2016. Experimental constraints on the formation of silicic magmas. Elements 12, 109–114.

Sigmarsson, O., Vlastelic, I., Andreasen, R., Bindeman, I., Devidal, J.L., Moune, S., Thordarson, T., 2011. Remobilization of silicic intrusion by mafic magmas during the 2010 Eyjafjallajökull eruption. Solid Earth 2 (2), 271.

Sigmundsson, F., Hreinsdóttir, S., Hooper, A., Arnadóttir, T., Pedersen, R., Roberts, M.J., Geirsson, H., 2010. Intrusion triggering of the 2010 Eyjafjallajokull explosive eruption. Nature 468 (7322), 426–430.

Sigmundsson, F., Einarsson, P., Bilham, R., 1992. Magma chamber deflation recorded by the Global Positioning System: the Hekla 1991 eruption. Geophys. Res. Lett. 19 (14), 1483–1486.

Soosalu, H., Einarsson, P., 2004. Seismic constraints on magma chambers at Hekla and Torfajökull volcanoes, Iceland. Bull. Volcanol. 66 (3), 276–286.

Sparks, S.R., Sigurdsson, H., 1977. Magma mixing: a mechanism for triggering acid explosive eruptions. Nature 267, 315–318.

Sturkell, E., Ágústsson, K., Linde, A.T., Sacks, S.I., Einarsson, P., Sigmundsson, F., Ólafsson, H., 2013. New insights into volcanic activity from strain and other deformation data for the Hekla 2000 eruption. J. Volcanol. Geotherm. Res. 256, 78–86.

Sverrisdottir, G., 2007. Hybrid magma generation preceding Plinian silicic eruptions at Hekla, Iceland: evidence from mineralogy and chemistry of two zoned deposits. Geol. Mag. 144 (04), 643–659.

Thordarson, T., Larsen, G., 2007. Volcanism in Iceland in historical time: volcano types, eruption styles and eruptive history. J. Geodyn. 43 (1), 118–152.

Tryggvason, A., Rögnvaldsson, S.T., Flóvenz, O.G., 2002. Three-dimensional imaging of the P- and S-wave velocity structure and earthquake locations beneath Southwest Iceland. Geophys. J. Int. 151 (3), 848–866.

Tryggvason, E., 1994. Observed ground deformation at Hekla, Iceland prior to and during the eruptions of 1970, 1980–1981 and 1991. J. Volcanol. Geotherm. Res. 61 (3), 281–291.

Waters, L.E., Lange, R.A., 2015. An updated calibration of the plagioclase–liquid hygrometer–thermometer applicable to basalts through rhyolites. Am. Mineral. 100 (10), 2172–2184.